An Empirical Study of GPR 3D Imaging Criteria

Tess X.H. Luo[a], Wallace W.L. Lai[a*], Ray K.W. Chang[a] and Dean Goodman[b]

[a.] Department of Land Surveying and Geo-informatics, The Hong Kong Polytechnic University, Hong Kong
[b.] Geophysical Archaeometry Laboratory Inc., 20014 Gypsy Ln, Woodland Hills, California 91364, USA

Declarations of interest: There is no interest to be declared. This research did not receive any specific grant from funding agencies in the public, commercial, or not-for-profit sectors.

Abstract: GPR has been widely acknowledged as an effective and efficient technique for imaging the subsurface and its 'filling'. But the process of constructing 3D GPR images (C-scans) is still subjective and mainly relies upon the operator's knowledge and experience. This study reviews the parameters that affect GPR imaging quality: namely, profile spacing (PS), slice thickness (ST) and interpolations. Feature characteristics that have a crucial influence on imaging quality were also identified. Through conducting 25 carefully designed empirical experiments on concrete as well as subsurface structures, the relationship between 3D imaging parameters and feature characteristics were observed. A general workflow was derived for GPR C-scan generation, which is analogous to the typical signal processing steps used in 2D radargram signal processing (Jol, 2009). Empirical values in workflow were based on the retrieval of known ground-truth data and comparison with the processed images, i.e. the closest to reality. Unlike 2D processing, the workflow for 3D is feature-oriented and case-specific, and the proposed workflow gives guidelines on suitable ranges for 3 major parameters when used in a variety of applications. It was identified that feature shapes and the ratios of feature size to radar footprint are of vital importance. With the proposed flowchart, the often vague "survey experience" is parametrized and standardized, and the upper and lower limits governing the generation of objective and trustworthy 3D GPR images are defined. This workflow for GPR 3D slice imaging also paves the way for GPR feature extraction and change detection commonly adopted in remote sensing.

Keyword: GPR**,** 3D imaging, imaging parameters, standardized workflow

1. Introduction

GPR is a non-destructive survey method that is based on the measured propagation and reflection of electromagnetic waves (Annan, 2004; Jol, 2009). After decades of development of theories and equipment, GPR has proven to be a time- and cost-efficient method for civil engineering subsurface imaging of, for example, utilities, rebar and voids (Annan, 2004).

Normally, A, B and C-scan are used for GPR data presentation in 1 to 3 dimensions, respectively. A C-scan, which is a representation of a 3D volume, images a horizontal section for a plane at certain depth. A widely applied presentation method for C-scans is horizontal slicing, in which each image is called a depth slice. In contrast, A-scan and B-scan images are vertical depth sections and provide details of the reflected waveform's characteristics, such as signal phase, amplitude and propagation velocity estimation. These characteristics are affected by the properties of the host media, but through forward and inverse modeling, the subsurface world can be reconstructed. A series of adjacent GPR profiles have to be inspected in order to determine the position and size of a subsurface target. Today, 3D C-scans are increasingly popular as they assist in interpreting the subsurface in a straightforward and easily understandable manner. Furthermore, many more advanced forms of 3D GPR representations were developed recently, for instance isosurfaces, semantic images based on energy or similarity, and feature enhancements (Böniger and Tronicke, 2010a; Böniger and Tronicke, 2010b; Leckebusch, 2003). They are all derivative presentations of full cover measurements in 3D and are aimed at supplying better

* corresponding author: ZS615, The Hong Kong Polytechnic University, Hung Hom, Hong Kong. email: wllai@polyu.edu.hk
Email address: tess.luo@connect.polyu.hk (Tess); wllai@polyu.edu.hk (Wallace); ray.chang@polyu.edu.hk (Ray); gal_usa_goodman@msn.com (Dean)

interpretations of 3D GPR volumes. A sequence of high-quality C-scans with reasonably accurate 3-dimensional measurements is an essential foundation for correctly depicting the subsurface world.

However, from a review of a large number of research studies conducted in recent decades (Lai, Dérobert, et al., 2017), it is obvious that 3D C-scans were first utilized in the 1990s (Goodman et al., 1995). The process of generating C-scans is still immature, and yet to be standardized. The parameters used for the generation of slices are mainly based on the experience of operators, which leads to inevitable human bias in imaging results (Millington and Cassidy, 2010). Because the choice of different parameter settings may result in completely different images, it is hard to determine whether the subsurface image is an accurate representation of the underground reality. Therefore, in order to optimize subsurface image and produce more accurate results, it is necessary to provide a standardized workflow for adjusting the parameters of C-scan processing. In addition, 4D measurements, which look at the difference in temporal subsurface changes by comparing C-scans at different times, require consistent and reliable images. Due to the variation of signals emitted by different antennas, it may be difficult to have repetitive GPR measurements at different times. The use of feature-oriented C-scans is a supplementary approach, since only semantic information about a feature is provided. Instead of interpreting complex waveforms and digits, a "health record" for buried infrastructure can be established from C-scans images with straightforward image processing, on condition that the feature condition is correctly described.

After decades of development, GPR 3D imaging has been widely applied in diverse fields of civil engineering: for example, in mapping underground utilities (Birken et al., 2002; Lai, Ho, et al., 2017; Metwaly, 2015; Ristic et al., 2009); measuring change of physical properties in materials (Kowalsky et al., 2005; Léger et al., 2014; Leucci et al., 2003); and inspecting structural conditions (Alani et al., 2013; Baker et al., 1997; Lai et al., 2013; Lai and Poon, 2012). More specifically, Nuzzo et al. (2002) imaged an archaeological site and pointed out that slice thickness is crucial as coarser slice thickness could lead to a less accurate depth estimation, although they did not suggest a suitable range for slice thickness. Grasmueck et al. (2013); Marchesini & Grasmueck (2015) imaged fractures and suggested that survey profile spacing should be no larger than ¼ wavelength, while Ghasemi and Abrishamian suggested the use of 3 profiles for delineating an anomalous body (Ghasemi and Abrishamian, 2007). Allroggen et al. (2015) stated that a dense profile spacing should be applied but only vaguely described other parameters used, while it was suggested that excessive data processing would introduce greater imaging variation. Topczewski et al. (2007) used linear interpolation to fill in gaps between profiles in order to better represent feature shape, while Barraca et al. (2016) applied rectangular interpolation with a radius equal to profile spacing. Cassidy et al. (2011) confirmed that practical experience plays a remarkable role in determining suitable values for imaging parameters. Some research has tended to skate over the process of 3D image production (Alani et al., 2013; Hugenschmidt and Kalogeropoulos, 2009; Porsani et al., 2012; Sagnard et al., 2016). Lualdi et al. (2003) point out that system resolution and antenna positioning accuracy are vital for high-quality 3D GPR imaging, while denser measurements ensure that image degradation is minimized. For acquired data, Goodman et al. (1995) summaries the processing flow of 3D time-slice reconstruction from a series of radargrams (B-scans) and focuses on 3 major steps: setting up the survey grid, cutting slices and interpolation. These steps are reflected in the above mentioned research, but a rigorous workflow, as used in 2D processing (Jol, 2009), is still missing.

In summary, how accurate 3D C-scans could be, depends on denser and more reliable 3D measurement points. GPR data acquisition is time consuming and labor intensive, and achieving full resolution imaging might be unrealistic in practice. This study aims at establishing a bridge connecting GPR resolution theory and survey practice, and strives to achieve a balance between acceptable imaging quality and survey workload for various imaging purposes. As the positioning accuracy is mainly determined by the system design, the post-processing stage cannot provide much image enhancement. Therefore, this study is focused upon 3D reconstruction from acquired GPR data. The chapter below reviews the concepts relating to GPR imaging quality.

2. GPR Resolution

2.1 GPR scattering theory

Scattering of light from electromagnetic waves contributes to the visible appearance of most features. The ratio of wavelength to a reflector's radius determines its visibility. Electromagnetic waves can be modelled in three forms: Rayleigh scattering, Mie scattering and optical scattering. Rayleigh scattering happens when the feature size is far smaller than the light wavelength, Mie scattering occurs if the feature size is similar to the light wavelength,; while optical scattering happens when the feature size is much larger than the light wavelength(Annan, 2004). Optical scattering yields optimal reflections while, on the contrary, targets are invisible in Rayleigh scattering. Fig 1. Illustrates the scattering concepts.

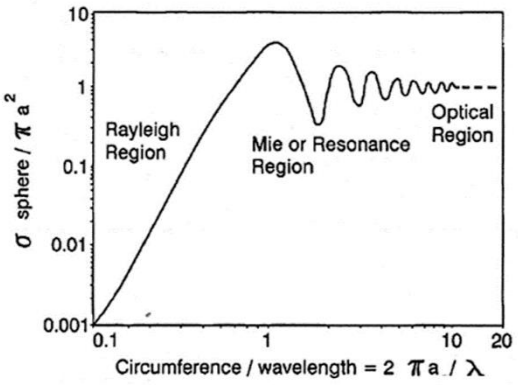

Fig.1. The illustration of scattering with feature sizes (Annan, 2004)

This study focuses on civil engineering applications involving far-field measurement at higher frequencies, broadly in the 400MHz to 3GHz range. The smallest target in this field of application is rebar in concrete, whose radius can be as small as 5mm. According to equation (1),

$$\lambda = \frac{v}{f} = \frac{c}{f\sqrt{\varepsilon'}} \tag{1}$$

where λ is the GPR wavelength; c denotes the traveling velocity of a GPR wave in free space, which is a constant of 0.2998 m/ns; f is the center frequency, and ε' denotes the host material's real part of complex permittivity.

Optical reflection forms the basis of most GPR applications in civil engineering. The deepest targets are buried within the upper few meters of the subsurface and, if the soil is non-conductive, are detectable even at higher frequencies. Additionally, as the radar signal penetrates deeper, higher frequencies tend to be absorbed and hence the center frequency is shifted to a lower region. In summary, when optical reflection occurs the target feature is "visible" to GPR.

Nevertheless, unlike satellite images-based remote sensing, the features present in GPR responses are not consistent with their true appearance. Post-processing and interpretation is needed in order to reconstruct the feature geometry. Zanzi & Arosio (2013) quantify the precision of rebar diameter estimation by using Radar Cross Section (RCS). According to the theory, the RCS ratio between cross-polarization and co-polarization varies with the target diameter (Ruck et al., 1970). As shown in Fig.2, the target diameter can be estimated by RCS in the lower frequency region, and the observable diameter range decreases in line with the increase of antenna frequency. For instance, when using a 600MHz antenna, the observable diameter range is 0.02m to 0.04m, which might be too small for the majority of subsurface utilities. In summary, even if a target is visible in GPR imaging, its size or diameter might not be precisely measurable with RCS in GPR sections. Dense 3D measurements can help in defining a proper 3D boundary for the target.

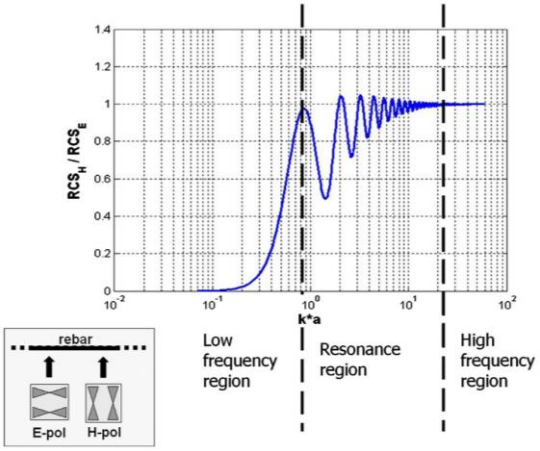

Fig. 2. RCS ratio between Cross-Polarization and Co-Polarization. k is the wavenumber and a is the cylinder radius (Zanzi and Arosio, 2013)

2.2 GPR spatial resolution

Once a feature is visible, the next question concerns how clearly it can be imaged. Where GPR imaging quality is concerned, spatial resolution and feature resolution need to be considered.

GPR spatial resolution is determined by characteristics such as radar signal, frequency, wavelength in materials, survey settings, and EM properties (Pérez-Gracia et al., 2010). Spatial resolution can be categorized into horizontal resolution and vertical resolution.

Horizontal resolution is defined as the capability of a GPR to distinguish 2 adjacent targets on the same plane, while vertical resolution describes the GPR system's ability to separate two adjacent features at different depths. When 2 targets are closely placed, large wavelengths would result in reflection superimposition. According to Nyquist's sampling equation, the resolution is considered to be ¼ of wavelength, although in field measurement a figure of ½ wavelength is more consistent with actual measured field resolution in many cases (Al-Qadi and Lahouar, 2005; Pérez-Gracia et al., 2010).

Whether the GPR system can separate 2 adjacent features at the same depth, is largely dependent on the footprint of the radar beam at a particular depth (Pérez-Gracia et al., 2009). Knowledge of the radiation pattern is therefore crucial for accurately estimating the GPR system's spatial resolution. Researchers have modelled GPR radiation patterns by measuring the main lobe and then provided illustrations showing that different kinds of antennas produce various radiation patterns (Jiao et al., 2000; Lambot et al., 2004; Pérez-Gracia et al., 2009).

The shape of the radiation pattern significantly affects the footprint of a GPR beam. A narrower beam width with smaller footprint provides better spatial resolution. Preliminary research done by Annan and Cosway (Annan and Cosway, 1992) established a simplified model of radar horizontal resolution, which was based upon the relationship between feature size and radar resolution. The footprint is usually estimated as the First Fresnel Zone (FFZ). There are various equations used to estimate the Fresnel zone in the far field (Leckebusch and Peikert, 2001; Leucci and Negri, 2006; Leucci et al., 2003). Among these equations, Eq. (2) is suggested in this study for its computational efficiency and stable performance (Pérez-Gracia et al., 2008). The estimation of spatial resolution is always rough as it concerns numerous factors, i.e. design of antenna, frequency, beam angle and host medium properties,

$$r = \sqrt{\left(\frac{v^2}{16f^2} + \frac{vz}{2f}\right)} \tag{2}$$

where r is the radius of FFZ, z denotes depth, f standard for dominant frequency, v is GPR wave velocity.

2.3 Dielectric contrast and attenuation

Another important aspect of slice quality is the feature visibility; whether the target feature can be distinguished from the background medium, which is governed by dielectric contrast (manifested as reflection coefficient) in equation (3).

$$R = \frac{\sqrt{\varepsilon_1} - \sqrt{\varepsilon_2}}{\sqrt{\varepsilon_1} + \sqrt{\varepsilon_2}} \quad (3)$$

Where R is the reflection coefficient across 2 vertical interfaces, ε denotes the dielectric constant/relative permittivity of the host medium.

Attenuation is another significant effect on a radar wave's amplitude. When a GPR signal penetrates a lossy medium, the amplitude decreases with depth. The attenuation rate depends on the electrical conductivity of the host medium. To visualize deeply buried features, a range gain function is applied to the data to compensate for the effects of attenuation. The use of different types of gain functions, however, can result in various "artificial" reflection intensities being unintentionally added to the subsurface image and an increase of noise alongside the signal. Knowledge of the attenuation rate in the real environment can help reduce errors and more accurately delineate the subsurface. The received signal intensities are transformed into colors and the scale used in that transformation process is very important because it describes the reflection contrast. A linear transformation that presents a true intensity contrast involves less operator interpretation, and it is suitable for a majority of GPR purposes, except in certain circumstances where signal exaggeration is required. The use of a non-linear color transform would actually increase the degree of human intervention and complexity in the image creation process. In this study, a linear color transform was applied in all cases.

3. Research Design and Methodology

This study is aimed, as much as possible, at reproducing the "subsurface world" through generating the most representative GPR C-scans. Based on the most crucial feature characteristics and GPR imaging parameters, the upper and lower limits for every parameter were defined for each application case. A relationship between GPR imaging and feature characteristics was investigated in order to construct an optimized combination for GPR imaging workflow.

3.1 Target features categorization

With reference to GPR principles and application case studies, subsurface geometries and material properties are 2 major parameters affecting imaging. Basically, a subsurface feature can be categorized into 2 main groups: continuous features with linear shapes, or local features with round or irregular shapes. The success of slice imaging depends on the dielectric contrast between the 2 materials being sufficient enough to record a reflection whose intensity can be imaged against the background noise level.

- Continuous linear features

Continuous reflections of linear features occur at transects across a series of parallel radargrams. Underground utilities and rebars in concrete are 2 major kinds of buried linear features. These linear features are presented as continuous reflections in C-scan displays.

- Local features

Local features are non-continuous structures, such as small voids or cracks, which appear in GPR radargrams as discrete reflections. The most crucial factor in identifying local features from GPR C-scans is the feature size.

3.2 3D C-scan parameters categorization

In line with the important characteristics of features discussed above, several crucial parameters in C-scan imaging are identified: the survey profile spacing, slice thickness, and interpolation.

3.2.1 Survey profile spacing (PS)

In GPR surveys, a denser GPR profile spacing can guarantee that all target features will fall within the radar's footprint. But how dense is dense enough? It is not realistic or practicable to acquire infinitely dense GPR profiles. Normally, the spacing of GPR profiles is no larger than the anticipated feature size or distance between adjacent features ("ASTM D6432-11," 2011). However, in practice there is always a need to balance between survey resolution and survey cost (Maas and Schmalzl, 2013). This study suggests a maximum threshold for profile spacing that can be applied while still providing a good enough resolution to identify subsurface features. The relationship between profile spacing and feature types is demonstrated in Fig. 3a.

3.2.2 Slice thickness (ST)

Depth slices show the radar reflection intensity over a certain thickness at a given depth. A single slice of a certain thickness presents a summed reflection within this depth range. Thicker slices produce more reflection energy, but this also introduces imprecision regarding feature depth. For non-overlapping slices, the choice of the depth error is at least half the slice thickness. For slice thicknesses that are much smaller than feature diameter, the feature cannot be fully delineated in a single slice. The use of an appropriate slice thickness is therefore important in C-scan imaging quality. An illustration of slice thickness is shown in Fig.3b.

3.2.3 Interpolation (IR)

Very often, survey profiles are not dense enough to map a full-resolution GPR image, even though full-resolution imaging has been shown to be superior (Grasmueck et al., 2005). Interpolations, such as inverse distance and kriging, are widely used to help with filling in gaps between survey grids. The selection of interpolation radius significantly affects C-scan resolution: a smaller radius preserves more true measurements while local extrema are maintained; in contrast, a larger radius creates data smoothing while details of smaller features can be lost. How the interpolation radius relates to GPR imaging resolution is not yet codified, hence this study attempted to be quantitatively analyzed in this paper. Two types of interpolation are discussed here: one is bi-linear interpolation, which means taking both orthogonal directions of GPR profiles into computation; while the other is linear interpolation, which is applied to single direction GPR profiles and interpolation is made primarily perpendicular to the profile direction. A schematic illustration of interpolation is shown in Fig 3c.

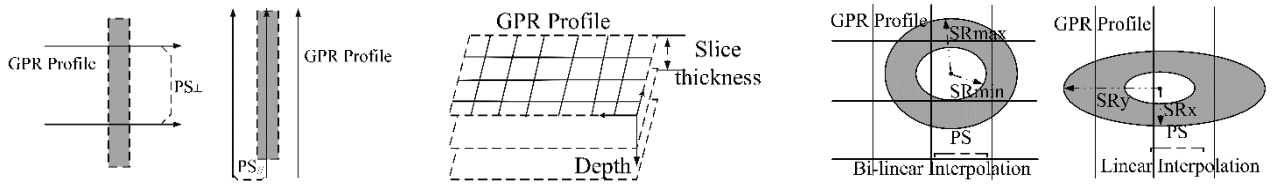

a b c

Fig.3. a) GPR profile spacing with a linear object: profile may perpendicular or parallel to the object orientation; b) illustration of slice thickness; c) illustrations of profile spacing and radius of associated bilinear/linear interpolation, with SRmax and SR min representing maximum and minimum acceptable search radius, respectively, while SRy and SRx denotes long axis and short axis of elliptical search radius in linear interpolation, respectively.

3.3 Empirical experiments

Having identified these important factors in terms of both feature characteristics and C-scan imaging parameters, four types of subsurface structures were designed:

A: concrete with rebar; B: underground utility; C: local features; D: complex combination

For each experiment, imaging parameters were adjusted and the resulting image resolution and feature reflection strength of C-scans were observed in order to determine appropriate ranges for each of the imaging parameters.

Before exploring the 3D C-scan process, basic 2D radargram processing was conducted. The velocity of the reflected radar waves was estimated by common offset velocity analysis (Sham and Lai, 2016), while the actual

frequency reflected by the feature was measured using a wavelet transform (Lai et al., 2014). Inspired by Annan (Annan, 2004), the 2D processing was simplified to avoid introducing unnecessary artificial signal noise. A processing flow is proposed for typical 2D processing of common offset GPR data (Annan, 2004; Jol, 2009). Several necessary steps were chosen for this study, as follows: dewow to remove the DC shift in the waveform; static correction to adjust time-zero; range gain for consistent amplitude contrast; bandpass and background removal; and frequency domain phase shift migration with independent velocity. When stacking B-scans into C-scans, the reflection intensity is transformed and presented as gray scale pixel images with linear color transforms. The color scale applied in each experiment was identical.

4. Results: A 3D imaging workflow

Based on the experience of conducting these empirical experiments, a workflow diagram is summarized in Fig. 4. Three levels of C-scan imaging are identified and presented in sequence in the workflow diagram. The first, in the green box, is the profile spacing (PS) which affects the horizontal resolution of C-scans. The second, in the blue box, is slice thickness (ST), which determines the vertical resolution. Antenna frequency, feature size and location depth all have effects on suitable thickness selection. The last level is the interpolation radius (purple box), which also has a crucial impact on the GPR C-scans' horizontal resolution.

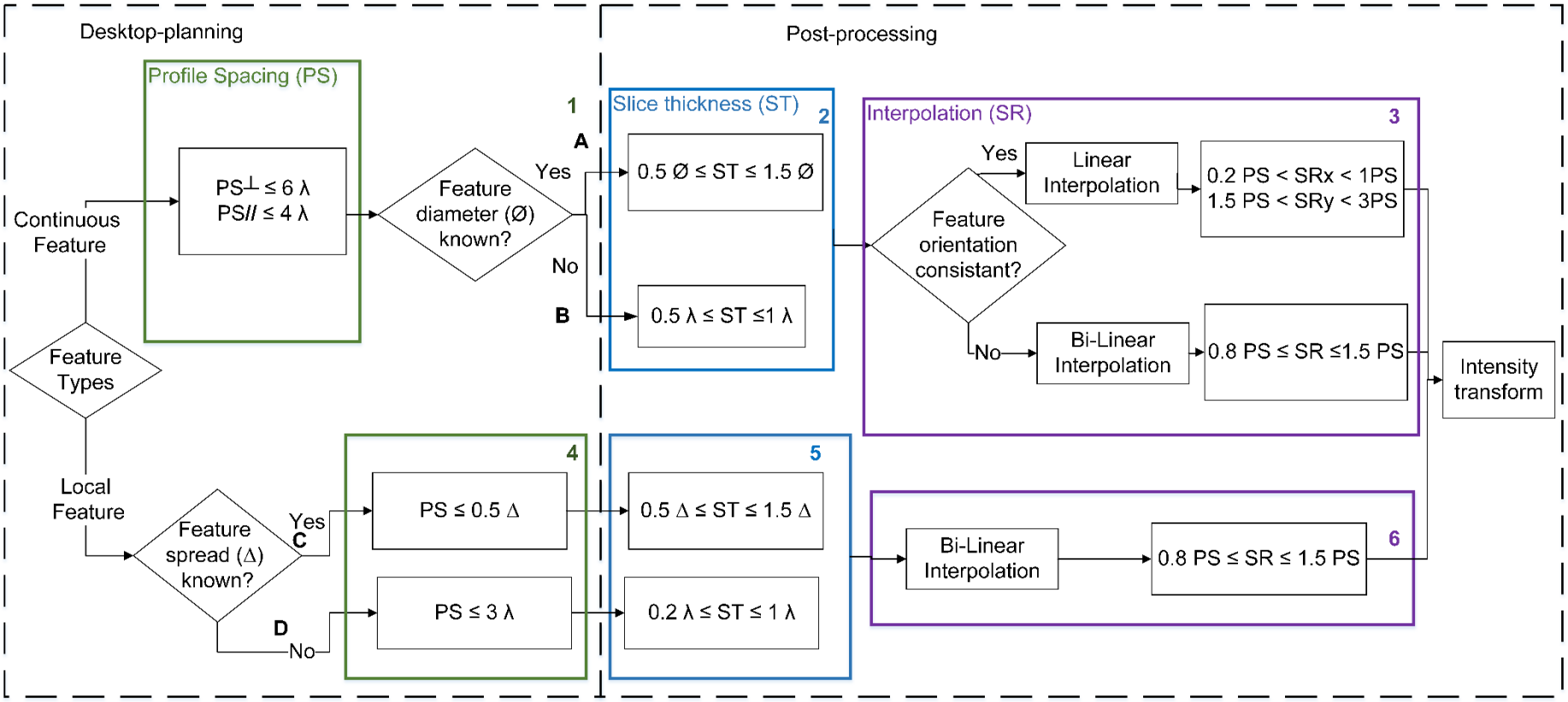

Fig. 4. 3D GPR imaging workflow based on empirical experiments. Remarks: (1) based on equation [1], where v can be determined by common offset velocity analysis (Sham and Lai, 2016), f can be determined by wavelet transform (Lai et al., 2014); (2) a feature spread (Δ) denotes feature's maximum spread along a traverse.

4.1 Representative Experiments

To detail illustrate the proposed workflow diagram in detail, 7 representative experiments were selected. Detail description on these 7 representative experiments are provided in Table 1 and Table 2.

Table 1 Experimental Specification

Workflow Path	Case	Site Photo	Survey Grid (↑)	Site Specification
A (Concrete)	Concrete Wall (CW) GSSI 2GHz		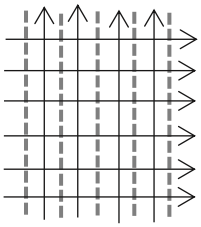	The concrete wall is placed in PolyU, with 2 layers of rebars embedded. The wall is 1.5*1.5m large.
	Concrete Slab (CS) GSSI 2GHz		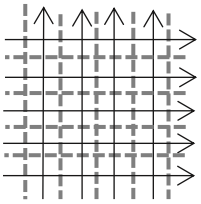	The concrete slab with 2 dense layers of rebars embed in is located in Ferry terminal of Hong Kong, the slab was 3.7*3m large.
	Stepped Steel (SS) GSSI 2GHz		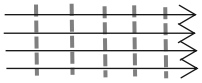	The specimen is placed in PolyU. 10 rebars stairs are embedded in the concrete block. Vertical/horizontal distance between each steel is 0.2/0.1m.
B (Underground Utility)	Back Lane (BL) IDS 600 and 200MHz		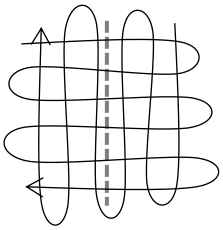	A school lane in PolyU, a drain pipe with 0.22 diameter was buried underneath. The site area is 50*5m.
	Island South (IS) GSSI 400MHz		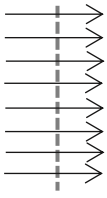	A pavement road section at Island South in Hong Kong. The road section was 200m long and 10m width. A rising main is buried below ground.

C (Local Feature)	Surface Void in Lab (LV) IDS 600MHz		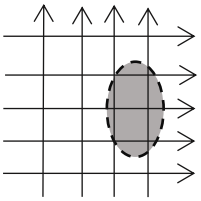	The void was placed in utility lab in PolyU. The void is 0.8*0.6*0.15 in size, and surrounded by garden soil. The whole survey area is 4.5*3m.
D (Complex)	Cathedral (CA) IDS 600MHz		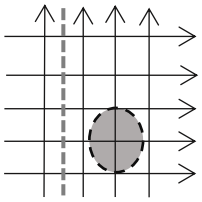	The cathedral is located in Central District of Hong Kong. The site area is 8*5m size concrete floor.
	Archeology Site (AR) GSSI 900MHz		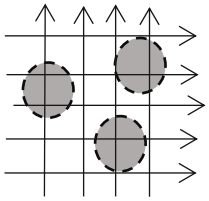	The site is located in Tung Chung of Hong Kong, filled with dry soil. The survey area is 20*10m large.

Table 2 Measured and calculated variables in survey A to D

Survey	Case	GPR Specification				Imaging Parameters			Feature Detail		
		f(GHz)	v(m/ns)	λ(m)	FFZ(m)	PS(m)	ST(m)	IR(m)	FS(m)	Depth(m)	FD(m)
A	CW	1.9	0.128	0.067	0.06	0.1	0.02	0.08	0.2	0.065	0.02
	CS	2.2	0.128	0.05	0.056	0.1	0.02	0.08	0.2	0.15	0.02
	SS	2.2(2^{nd})	0.128	0.058	0.055	0.1	0.008	0.07	0.1	0.085	0.01
		2.6(5^{th})	0.106	0.04	0.095	0.1	0.015	0.07	0.1	0.135	0.01
B	BL	0.210	0.105	0.48	0.43	0.5	0.301	0.4	\	0.62	0.2
		0.496	0.0815	0.163	0.24	0.5	0.245	0.4	\	0.62	0.2
	IR	0.710	0.101	0.208	0.108	1	0.2	0.7	\	0.55	0.2
C	LV	0.481	0.104	0.207	0.104	0.3	0.1	0.21	\	0.1	0.6
D	CA	0.680	0.098	0.14	0.09	0.5	0.116	0.3	\	0.3	0.5
	AR	0.780	0.139	0.178	0.216	0.5	0.1	1	\	0.5	\

Remarks: f is frequency measured with Lai et al. (2014); v is measured velocity estimated by Sham & Lai (2016), λ and FFZ are calculated wavelength and calculated radar footprint, respectively; PS, ST IR, FS, D, FD are profile spacing, slice thickness, interpolation radius, feature spacing, feature depth and feature diameter, respectively.

4.2 Continuous Features (Survey A/B)

The shapes and orientations of profiles to object alignment are of vital importance when mapping continuous features.

4.2.1 Profile spacing for continuous feature (Box 1 in Fig.4)

Different profile spacing settings were tested for imaging the concrete wall (CW) and concrete slab (SW), in order to investigate the minimum requirements for GPR profile spacing, as shown in Fig. 5. It is widely accepted

that the denser the GPR profiles acquired, the higher the GPR imaging resolution achieved, but there is no lower boundary on profile spacing. In principle, the profile spacing should be smaller than half the rebar spacing so that both the gaps and rebars can be mapped. In all civil engineering applications, three profiles for one feature can guarantee high-quality C-scans. When working in larger survey areas, data collection of such dense profiles is time consuming and labor intensive. Then a trade-off would be to reduce the number of profiles and sacrifice a higher resolution, while ensuring that the target can be still mapped.

Figs. 5(a) and (c) show the imaging result when profile spacing is equal to rebar spacing, which allows each rebar to be distinguished clearly. When the profile spacing is twice that of the rebar spacing, obvious artificial error occurred: each rebar was interpolated to be straight, as shown in red circled areas in Fig. 5(b) and (e). Although the general areas with a stronger intensity were still mapped, they were shifted in position. In principle, at least two reflectors are needed for the definition of one linear shaped rebar. Although there were insufficient GPR profiles acquired, the general subsurface scene could nevertheless be imaged by interpolation without loss of imaging clarity.

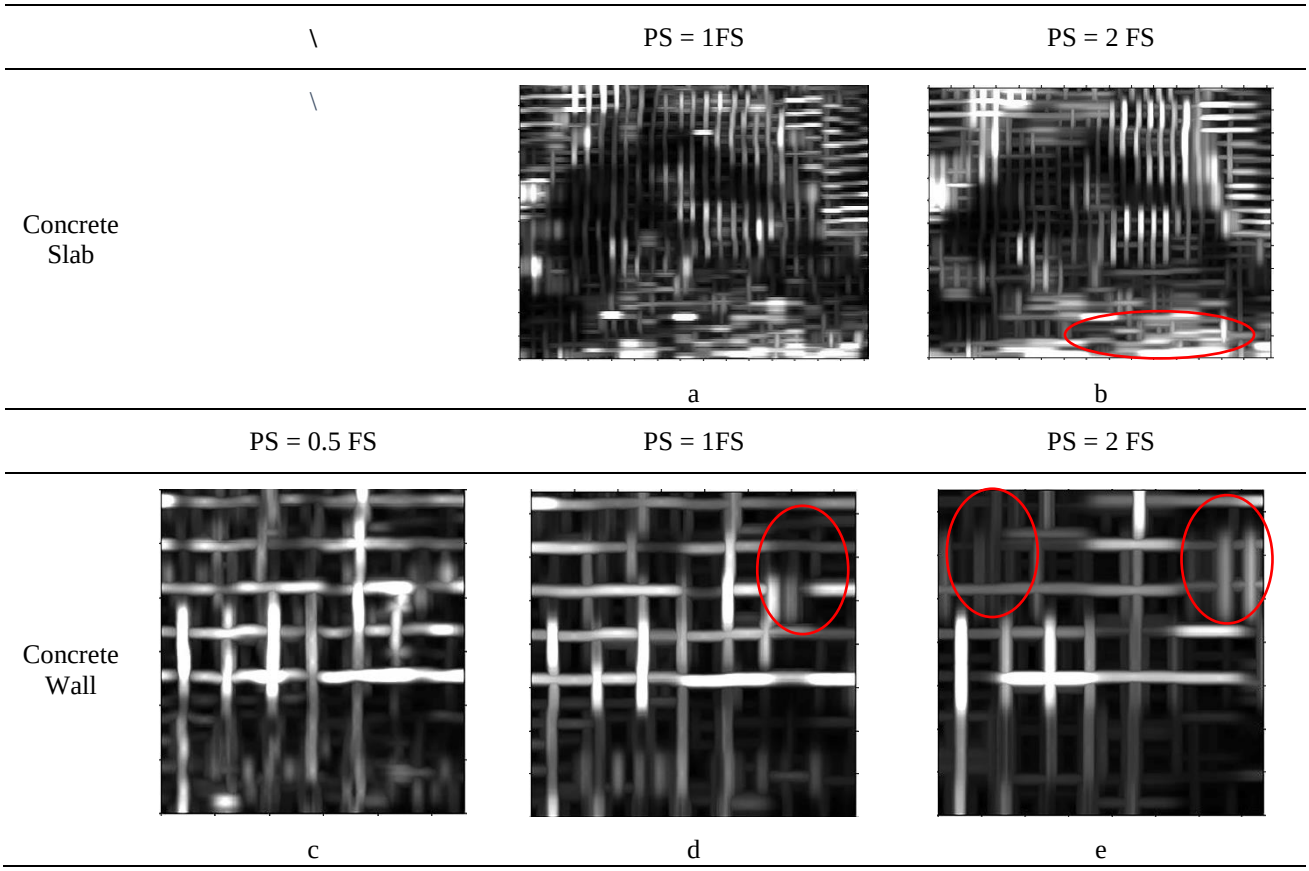

Fig. 5 (a) and (b) are C-scans of concrete slab with profile spacing being 1 or 2 times feature spacing; c-e are C-scans of concrete wall with profile spacing being 0.5, 1 or 2 times feature spacing.

However, normally known and consistent feature spacing only exist in concrete and rebar mapping. In this case, the rebar diameter is normally far smaller than the rebar spacing, and rebar spacing – 0.1 to 0.2m – is often significantly larger than multiple times of radar wavelength. When feature size and feature spacing are both unknown (i.e. Path B in Fig. 4), the radar's wavelength is then the only factor taken into consideration when computing the GPR horizontal resolution, based on the principle of radar footprint. As discussed in Section 2, the profile spacing should be ¼ of wavelength. In Path A experiments (CS and CW), the wavelengths of the 1.9-2.2GHz radars were 0.05-0.06m, which being smaller than the rebar spacing was still acceptable for imaging such linear features. In addition, diameters of linear features are very often small (i.e. diameters of rebar and utility), compared with their lengths. Applying diameter as reference to define survey profile spacing maybe not feasible. Thus, wavelength is focused to determine the suitable range of profile spacing.

The road section in Island South (IS) was an ideal example for validating the imaging performance of different profile spacings for mapping single linear shaped features, as shown in Fig. 6. When mapping continuous underground utilities within larger areas, less dense profiles can be used.

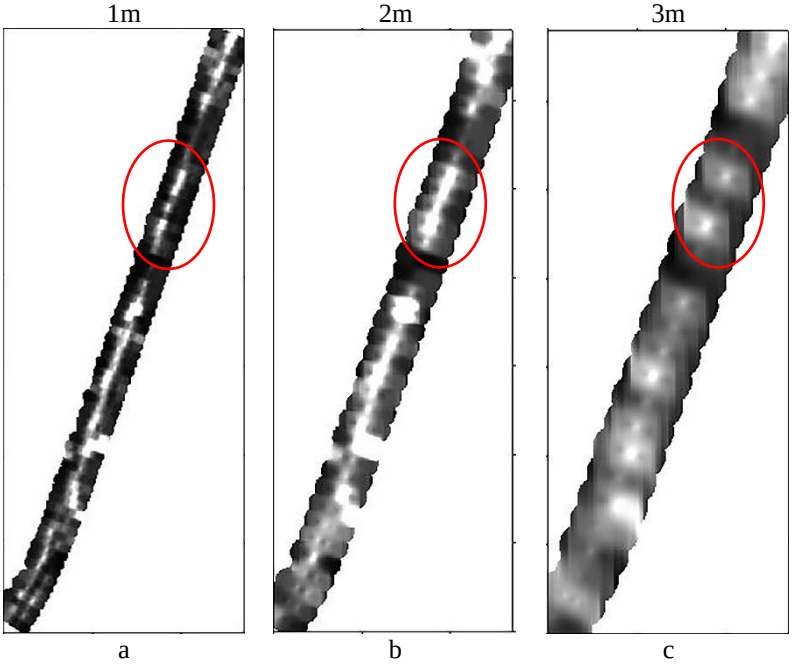

Fig. 6. C-scans of Island Road with a:1m, b:2m, and c:3m profile spacing.

When comparing the 3 generated results shown in Fig. 6, there is clearly an upper limit to profile spacing. According to Table 2, the 1-3m profile spacing of the IS case study is significantly larger than the feature (the pipe) diameter, and much larger still than the radar footprint, and even though the position of the pipe was located, its size was exaggerated. However, the discontinuities in the pipe (circled in red in the 1m C-scans), which were confirmed to be caused by leakage or defects, were connected in the 2m C-scans. The post-image computation resulted in an inaccurate visualization of the subsurface situation.

Besides, as the angle between profiles and a linear object has a significant impact upon GPR response, the choice suitable thresholds should be discussed from two aspects: the best and worst situation. In the best case, profiles are perpendicular to a linear object and a larger profile spacing is acceptable. In terms of the worst case, profiles are parallel with a linear object, which means that the response of the GPR will not be obvious enough and a smaller profile spacing is required. If the survey grid is orthogonal, or the angle between GPR profiles and the linear object is an acute one, then the suitable range of profile spacing will fall within the those of the best and worst cases.

In sum, a suggestion for the selection of a suitable profile spacing is as shown in Rule (a).

$$\begin{cases} PS_{\perp} \leq FS, & feature\ spacing\ known\ and\ consistant \\ PS_{\perp} \leq 6\lambda, & feature\ spacing\ unknown\ or\ inconsistant \\ PS_{//} \leq 4\lambda, & feature\ spacing\ unknown\ or\ inconsistant \end{cases} \quad \text{(a)}$$

4.2.2 Slice thickness for continuous features (Box 2 in Fig. 4)

The stepped steel (SS) specimen was used to illustrate and describe the factors affecting slice thickness selection (Fig. 7), and a consistent gray scale was maintained for these C-scans. For the stepped steel, the background material is concrete, which is relatively more homogenous than a typical underground environment, and the steel bars were evenly distributed.

As shown in Table 1, rebars were buried with increasing depth, and the 2nd and the 5th rebars were selected to show the different imaging performance resulting from the variation of imaging parameters at different depths. It is obvious that the apparent size of the imaged steel rebars was larger with larger slice thicknesses, but slices with a thickness smaller than 1 rebar diameter produced better imaging results, and the size of the imaged rebar is closer to that of reality. In particular, in deeper locations ((a) column) where the GPR signal is significantly attenuated, an excessively small slice thickness results in the mapping of insufficient energy to present a solid feature. Conversely, an excessively large slice cannot provide an accurate representation of the object's depth, due to the lack of vertical resolution. In shallower areas ((b) column), the exaggeration of mapped rebar size was less significant than that in the deeper area. The footprint of the GPR increases with depth, but also causes the horizontal resolution to decrease with depth. These 2 observations illustrate the principle that GPR horizontal resolution depends upon the ratio of feature size and radar footprint.

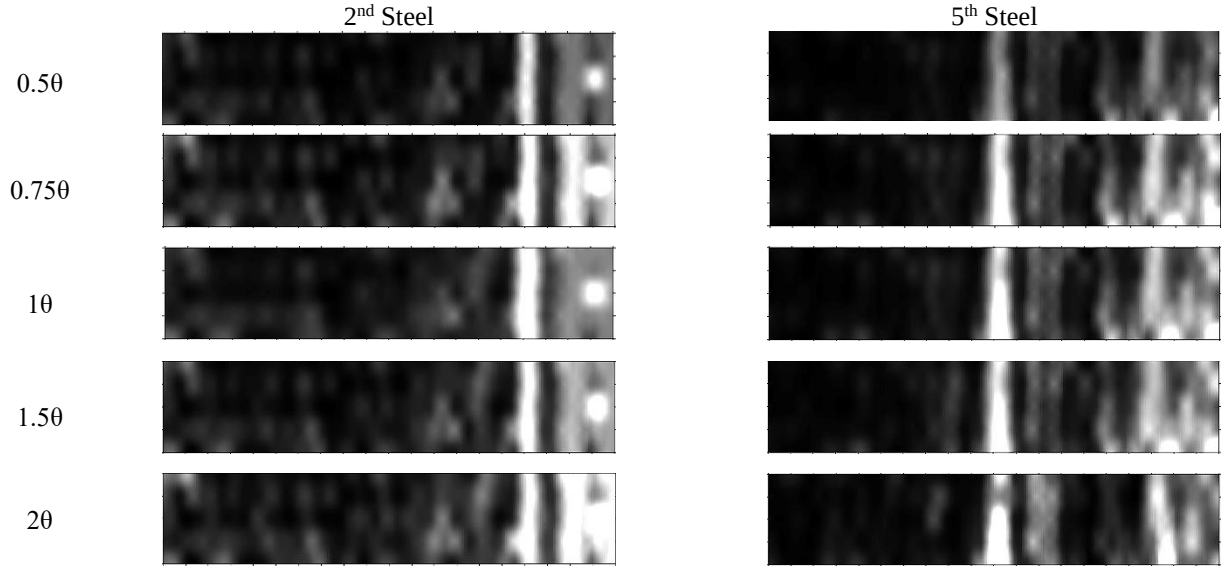

Fig. 7. C-scans of the 2nd ((a) column) and 5th ((b) column) steel bar with different slice thicknesses.

Another crucial factor affecting GPR resolution is the radar wavelength. The case of mapping underground utilities in the back lane at PolyU provides a nice example for illustrating the choice of an appropriate slice thickness for a known feature size and radar wavelength. With the exception of the 2 known utilities buried at the site, we had limited knowledge of the subsurface environment of the entire road (as Table 1). The GPR data were collected with positioning provided by an auto-tracked robotic total station. Fig. 8 illustrates the different C-scan imaging performance with changing slice thickness.

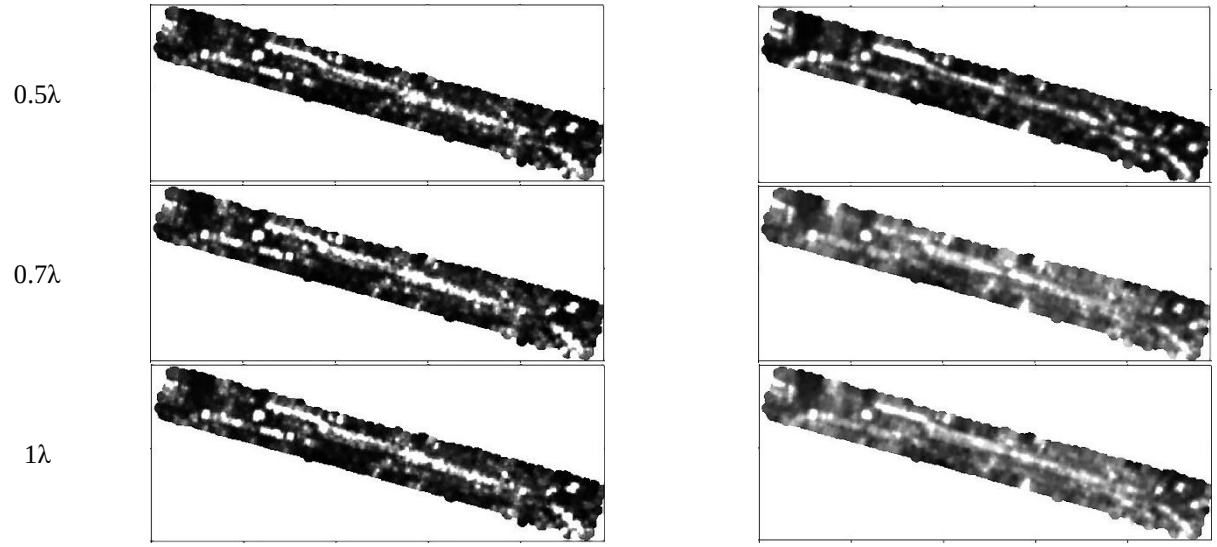

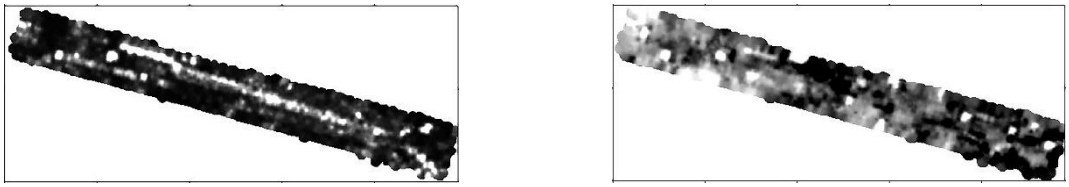

Fig. 8. C-scans of PolyU back lane of 490MHz from 600MHz antenna (a) and 210MHz from 200MHz antenna (b), with thickness from 0.5λ to 2λ

As the antenna footprint depends on its frequency (wavelength), the effect of changing the slice thickness produced different results in C-scans obtained from the two frequencies. As illustrated in Fig. 8, various thickness settings produce similar results when using a higher frequency (600MHz) antenna. With the 200MHz antenna, the image of the utility gradually faded out when the slice thickness was smaller than 1 wavelength. According to Table 2, the number of 1λ of 210MHz GPR data was 2 times than the estimated pipe diameter, but even 2λ of 600MHz data was much smaller than the pipe's diameter. The imaging results correlate well with Fig. 7, thus confirming that the slice thickness should not be larger than the feature size.

Drawing conclusions from these experiments, a guideline for suitable slice thickness is presented below as Rule (b).

$$\begin{cases} 0.5\emptyset \le ST \le 1.5\emptyset, & feature\ size\ known \\ 0.2\lambda \le ST \le 1\lambda, & feature\ size\ unknown \end{cases} \quad \text{(b)}$$

4.2.3 Interpolation for continuous feature (Box 3 in Fig. 4)

Another observation is that the horizontal resolution is also affected by the interpolation radius applied. In GPR 3D survey, local interpolation methods are widely applied. When maintaining other parameters and only changing the interpolation radius, significantly different imaging results can be obtained (Fig. 9). When the interpolation search radius was larger than 2 times the profile spacing, 2 steel bars almost merged into one in a C-scan image. In cases such as the mapping of steel rebars in concrete, attention should be paid to the horizontal distance between 2 targets when defining the interpolation radius, and it should be no larger than the distance between 2 adjacent features.

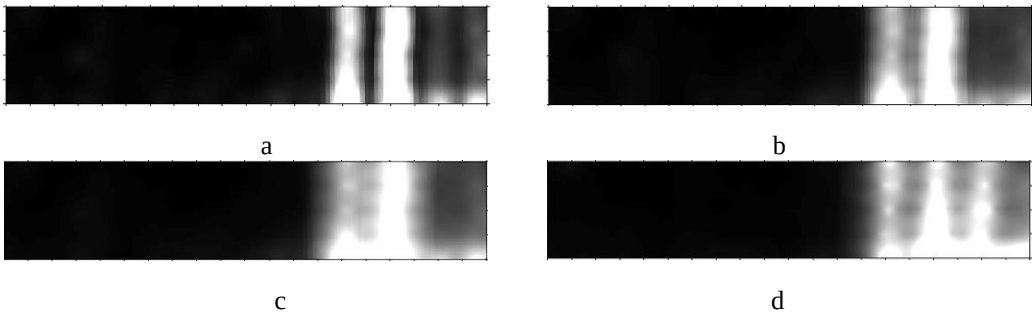

Fig. 9. C-scans of upper steel bar with different interpolation radiuses (a-d show profile spacings of 0.6, 1, 1.5, and 2 respectively).

The orientation of the GPR profiles has a remarkable impact on the accuracy of GPR velocity estimation. A profile that is perpendicular to a linear feature's orientation provides the most accurate measurements (Xie et al., 2018). If the alignment of a linear feature is known, then collecting data perpendicular to it is recommended. For surveys collected in both directions, decoupling cross grid profiles can enhance imaging of linear features.

The concrete wall (CW) was used as an example to demonstrate the decoupling of cross profiles with linear interpolation. The performance of different search ranges in linear interpolation is shown in Fig. 10. Specifically, the shorter axis refers to the radius perpendicular to profile orientation, while the longer axis represents the radius in line with the profile orientation.

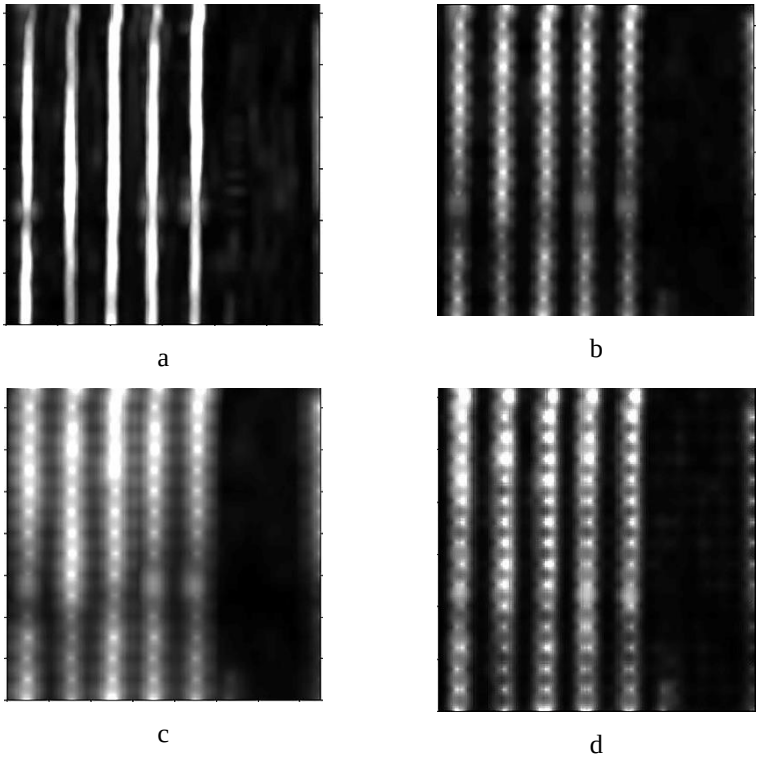

Fig. 10. C-scans of concrete wall with different interpolation radiuses (a-d are 0.2x2y; 0.6x1y; 1x2y and 1xy times profile spacing respectively).

Therefore, a guideline for selecting a suitable interpolation radius when mapping linear features is as shown in Rule (c):

$$\begin{cases} 0.2PS \le SR \le 1PS, & profile\ perpendicular\ to\ feature\ orientation \\ 0.8PS \le SR \le 1.5PS, & mis-oriented\ profiles \end{cases} \quad (c)$$

where SR (search radius) refers to short axis of linear interpolation.

4.3 Local Feature (Path C/D)

Since there are no concerns over "connectivity" between GPR survey profiles when imaging local features, more attention should be paid to estimating the correct size of the feature. In view of this desired imaging objective, emphasis is put on defining rules for interpolation.

4.3.1 Bilinear interpolation for local features (Box 6 in Fig. 4)

The surface voids created in the utility lab were used to illustrate how local features can be imaged with GPR. In this case, bi-linear interpolation was applied to allocate an even weighting to measurements in all directions. Fig. 11 compares the C-scans of surface voids with different interpolation settings. The effect of interpolation radius on feature size was studied using the case of surface voids. For local feature which are not necessary in regular shape, diameter is not proper in describing their size. Maximum feature spread along a GPR traverse is applied to represent the feature size.

When void size is not estimated, it is desirable to apply interpolation with a radius of 0.7-1 times the profile spacing. As demonstrated in Fig. 11, the imaged voids were closer to their actual size when a radius equal to half the profile spacing was used, with the achievable horizontal resolution maintained as well as was possible. In contrast, the void became increasingly smoothed when the radius reached 1 profile spacing or larger. A proposed rule for imaging local features is shown as Rule d.

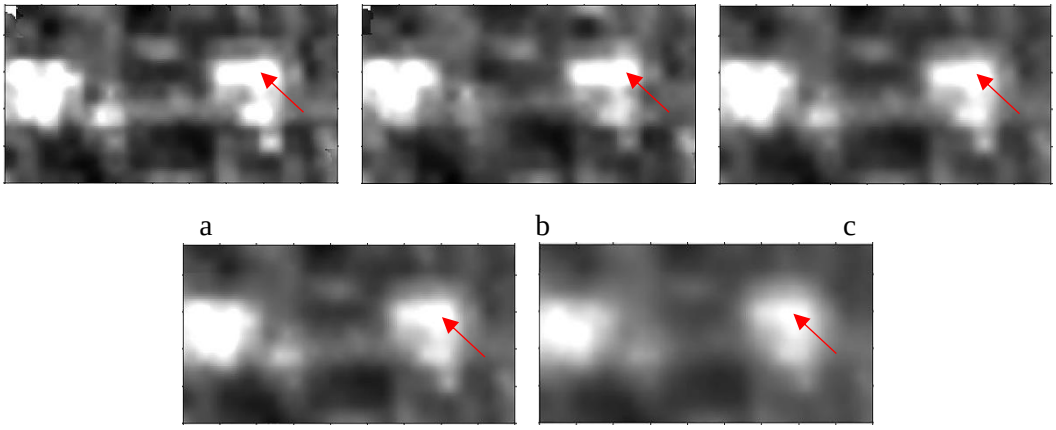

Fig. 11. a-e are C-scans of voids with interpolation set at 0.5, 0.7, 1,1.5, and 2 times profile spacing, respectively

$$\begin{cases} PS < 0.5\Delta \\ PS \leq 3\lambda \end{cases} \rightarrow \begin{cases} 0.5\Delta \leq ST \leq 1.5\Delta \\ 0.2\lambda \leq ST \leq 1\lambda \end{cases} \rightarrow 0.8PS \leq SR \leq 1.5PS \quad \text{(d)}$$

In addition, owing to the development of auto-track positioning technology—GPR armed with GPS or tracked total-station providing real-time positioning—when mapping large areas, GPR survey can be conducted without the need to follow pre-planned grids. If it is difficult to carry out GPR survey in two orthogonal direction, or no prior knowledge of the feature is possible, then bilinear or even multi-directional interpolation is recommended to avoid the introduction of artificial reflections. Positioning errors, whether occurring in grid-guided survey or auto-positioning survey, are systemic errors that are hard to rectify in post-processing.

4.3.2 Decouple interpolation for local features (Box 456 in Fig. 4)

For more complex situations, for instance involving the coexistence of linear and local objects about which little is known (survey D), the bottom workflow in the flowchart is proposed. The experimental work at St. John's Cathedral (CA) was used to validate this path. In this case, the GPR survey was conducted in both directions, and linear interpolation aimed at decoupling the two orientation profiles was utilized. Fig. 12 presents the C-scans resulting from the cathedral survey, with different combinations of short or long axis of interpolation radius. As there was a linear shaped feature on the right of the survey area, it is obvious that a circular shaped interpolation radius performs better in this case.

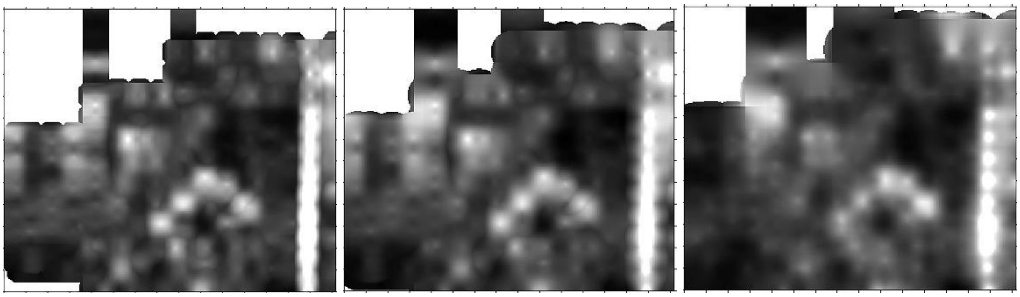

Fig. 12. a-c are C-scans at same depth of Cathedral underground with interpolation being 0.8x1.5y, 1x1.5y, and 1.5xy times profile spacing, respectively.

A higher frequency and smaller profile spacing were used at the archeological site and smaller features were delineated with higher resolution C-scan images. In this case, although decoupling of two directional profiles and image mathematics were applied, adjacent features were still distinguishable. When comparing the C-scans of 1xy and 1x2y, the imaging result are very similar, as shown in Fig. 13. If the depiction of feature linearity is not a priority, then the decoupling of GPR profiles of different orientations might not yield significant improvement in the imaging of local features. Instead, the size of interpolation radius has a far more obvious

effect on C-scan generation. When the interpolation radius falls within the 0.8-1.5 profile spacing, the generated C-scans do not show significant difference, which correlates well with rule (d).

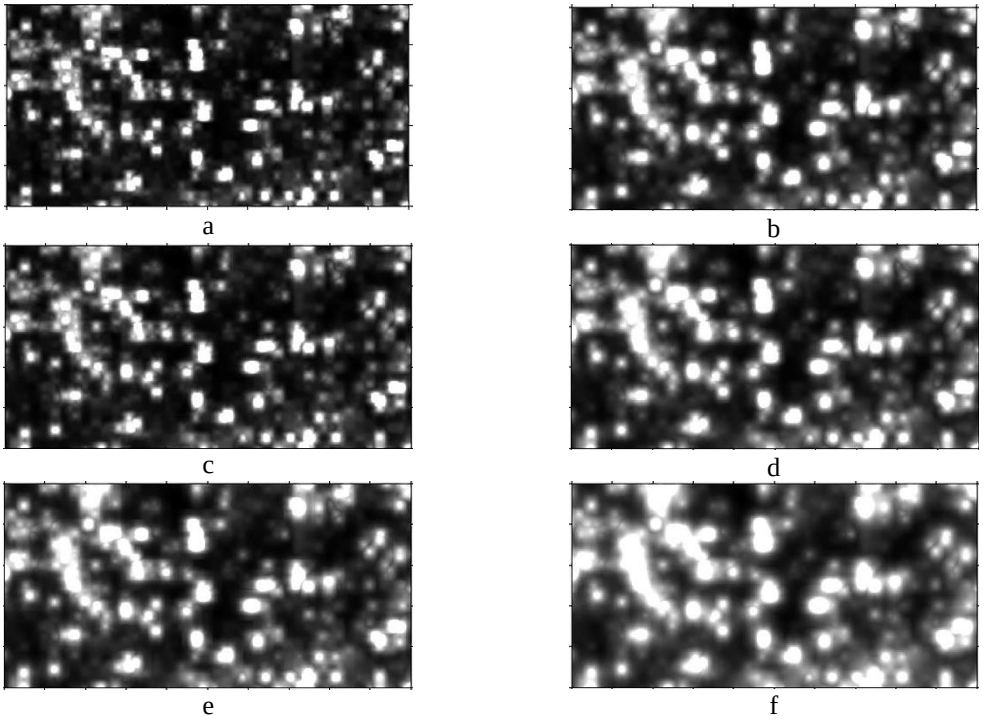

Fig. 13. C-scans of the archaeological site with different interpolation radiuses (a-f is 0.6_{xy}, 0.8_x2_y, 1_{xy}, 1_x2_y, 1.5_{xy} and 2_{xy} times profile spacing, respectively).

5. Discussion

According to the findings and generalized rules, the process of GPR 3D imaging is feature oriented and the parameters of the process are interrelated. Generally speaking, there is no one-size-fits-all standard; instead a guided thought process, which integrates the physics of GPR imaging with survey operation experience, is required.

5.1Objective-oriented process

The creation of GPR C-scans can be subjective, as the process is a "black box" that interprets and visualizes recorded GPR signals and converts them into semantic images. As a consequence, it is also an objective-oriented process and there are lower and upper range limits for each imaging parameter. Also, the tolerance on the value of each parameter depends on the feature being investigated and the intended end user of the survey results. There are also trade-offs between "detecting the feature" and "mapping the feature". The lower limit of a suitable range provides the best imaging results, with the feature's geometry being depicted closest to the physical reality. The upper limit of a suitable range does not necessarily result in significantly degraded images, and in some surveys a degree of image degradation is acceptable. For instance, in the concrete slab (CS) case shown in Fig. 4, with the help of perpendicular GPR profiles and linear interpolation (box 3 in Fig. 4), even when a larger profile spacing is utilized, the buried rebar can still be imaged, albeit with some errors. This was possible due to the idea that only two points are needed to define a line. But if the survey is targeted at the detection of corrosion in a concrete slab, it is not necessary to have each rebar clearly imaged, and a larger profile spacing and lower image quality, reflecting the upper limit of a suitable range, can be applied. In conclusion, there is some tolerance available when defining the suitable range for each parameter, in order to maintain a fit-for-purpose survey.

5.2Interrelated parameters

Though many researchers suggest denser survey profiles, it was observed that when mapping linear features such as rebar, a coarser profile spacing can still be acceptable. Based on equation (1), when mapping shallower areas, the profile spacing should not be larger than 3 times the radar footprint or wavelength. In this way, the time and cost required to conduct the GPR survey can be significantly reduced (box 1 in Fig. 4).

In terms of slice thickness, the empirical experiment on rebar in concrete confirmed that the depth accuracy for C-scans is half the slice thickness, and it must be kept in mind that a thinner slice thickness reduces depth resolution errors. In addition, in many civil engineering applications, such as imaging concrete with higher frequency antennas when the targeted reflection intensities are strong, a larger or smaller slice thickness does not necessary perform well. On the contrary, when working with lower frequency GPR in situations where the feature size is comparable to the wavelength, a large slice thickness would result in a blurred image of the feature, while an excessively small slice thickness would have insufficient reflection intensity to depict the feature. Therefore, it is believed that slice thickness should be determined according to the ratio of feature size to radar footprint. With reference to Table 2, the slice thickness of all representative cases was smaller than the radar wavelength, and the most satisfactory results were recorded when the slice thickness was similar to the feature's diameter (box 2 in Fig. 4). Based on these empirical experiments, a slice thickness of at least half a wavelength is suggested when the feature diameter is unknown.

Another important imaging parameter is interpolation. If the alignment of a linear feature is consistent, then an elongated shaped radius with linear interpolation is suggested, so as to add weighting to measurements on profiles perpendicular to the feature alignment. It is indicated in Goodman (2017) that applying linear interpolation and decoupling cross profiles can provide better images when depicting linear shaped features. However, if the feature alignments are mis-oriented, or one is mapping a local feature, a larger search radius is helpful for eliminating anomalies. However, an excessively large search radius may result in undue image smoothing, while many unnecessary scatterers could be imaged if the radius is too small. Hence, it may be difficult to maintain a balance between retaining true measurements while smoothing tiny local speckles.

6. Conclusion

Specific rules provided in the workflow were summarized using 25 experiments, and it was demonstrated that the construction of GPR 3D images (C-scans) should be feature-oriented and case-specific. A standardized GPR imaging workflow that can produce convincing images with few human judgements is beneficial to the survey industry. This study reviewed GPR imaging theories as well as important parameters that affect GPR imaging quality, and identified the feature characteristics that have a crucial influence on imaging quality. A relationship between feature and imaging parameters was established so as to define a suitable range for each parameter. When reliable C-scans can be produced using a standardized workflow, more meaningful interpretations can then be based on those images, thus bringing the unseen subsurface world into view.

Acknowledgement

The authors wish to thank Mick Atha for his efforts in English editing. Great appreciation also goes to reviewers for their constructive comments.

Reference

Al-Qadi, I., & Lahouar, S. (2005). Measuring layer thicknesses with GPR–Theory to practice. *Construction and Building Materials, 19*(10), 763-772.

Alani, A. M., Aboutalebi, M., & Kilic, G. (2013). Applications of ground penetrating radar (GPR) in bridge deck monitoring and assessment. *Journal of Applied Geophysics, 97*, 45-54.

Allroggen, N., van Schaik, N. L. M. B., & Tronicke, J. (2015). 4D ground-penetrating radar during a plot scale dye tracer experiment. *Journal of Applied Geophysics, 118*, 139-144. doi:10.1016/j.jappgeo.2015.04.016

Annan, A., & Cosway, S. (1992). Simplified GPR beam model for survey design *SEG Technical Program Expanded Abstracts 1992* (pp. 356-359): Society of Exploration Geophysicists.

Annan, A. P. (2004). *Ground Penetrating Radar Applications, Principles, Procedures*. Mississauga, Canada: Sensors and Software.

ASTM D6432-11. (2011). *Standard Guide for Using the Surface Ground Penetrating Radar Method for Subsurface Investigation*.

Baker, J. A., Anderson, N. L., & Pilles, P. J. (1997). Ground-penetrating radar surveying in support of archeological site investigations. *Computers & Geosciences, 23*(10), 1093-1099.

Barraca, N., Almeida, M., Varum, H., Almeida, F., & Matias, M. S. (2016). A case study of the use of GPR for rehabilitation of a classified Art Deco building: The InovaDomus house. *Journal of Applied Geophysics, 127*, 1-13. doi:10.1016/j.jappgeo.2016.02.002

Birken, R., Miller, D. E., Burns, M., Albats, P., Casadonte, R., Deming, R., . . . Oristaglio, M. (2002). *Efficient large-scale underground utility mapping in New York City using a multichannel ground-penetrating imaging radar system.* Paper presented at the Ninth International Conference on Ground Penetrating Radar (GPR2002).

Böniger, U., & Tronicke, J. (2010a). Improving the interpretability of 3D GPR data using target–specific attributes: application to tomb detection. *Journal of Archaeological Science, 37*(4), 672-679. doi:10.1016/j.jas.2010.01.013

Böniger, U., & Tronicke, J. (2010b). *Symmetry based 3D GPR feature enhancement and extraction.* Paper presented at the Ground Penetrating Radar (GPR), 2010 13th International Conference on.

Cassidy, N. J., Eddies, R., & Dods, S. (2011). Void detection beneath reinforced concrete sections: The practical application of ground-penetrating radar and ultrasonic techniques. *Journal of Applied Geophysics, 74*(4), 263-276. doi:10.1016/j.jappgeo.2011.06.003

Ghasemi, F. S. A., & Abrishamian, M. (2007). A novel method for FDTD numerical GPR imaging of arbitrary shapes based on Fourier transform. *NDT & E International, 40*(2), 140-146.

Goodman, D. (2017). GPR-SLICE Software Manual.

Goodman, D., Nishimura, Y., & Rogers, J. D. (1995). GPR (Ground Penetrating Radar) Time Slices in Archaeological Prospection. *Archaeological Prospection, 2*(January), 85-89.

Grasmueck, M., Quintà, M. C., Pomar, K., & Eberli, G. P. (2013). Diffraction imaging of sub-vertical fractures and karst with full-resolution 3D Ground-Penetrating Radar. *Geophysical prospecting, 61*(5), 907-918. doi:10.1111/1365-2478.12004

Grasmueck, M., Weger, R., & Horstmeyer, H. (2005). Full-resolution 3D GPR imaging. *Geophysics, 70*(1), K12-K19.

Hugenschmidt, J., & Kalogeropoulos, A. (2009). The inspection of retaining walls using GPR. *Journal of Applied Geophysics, 67*(4), 335-344. doi:10.1016/j.jappgeo.2008.09.001

Jiao, Y., McMechan, G. A., & Pettinell, E. i. (2000). In situ 2-D and 3-D measurements of radiation patterns of half-wave diphole GPR antennas. *Journal of Applied Geophysics, 43*, 69-89. doi:S0926-9851 99 00048-8

Jol, H. M. (2009). *Ground Penetrating Radar Theory and Applications*: Oxford: Elsevier.

Kowalsky, M. B., Finsterle, S., Peterson, J., Hubbard, S., Rubin, Y., Majer, E., . . . Gee, G. (2005). Estimation of field‐scale soil hydraulic and dielectric parameters through joint inversion of GPR and hydrological data. *Water resources research, 41*(11).

Lai, W.-L. W., Kind, T., Kruschwitz, S., Wöstmann, J., & Wiggenhauser, H. (2014). Spectral absorption of spatial and temporal ground penetrating radar signals by water in construction materials. *NDT & E International, 67*, 55-63. doi:10.1016/j.ndteint.2014.06.009

Lai, W. L., Kind, T., Stoppel, M., & Wiggenhauser, H. (2013). Measurement of Accelerated Steel Corrosion in Concrete Using Ground-Penetrating Radar and a Modified Half-Cell Potential Method. *Journal of infrastructure systems, 19*(2), 205-220. doi:10.1061/(asce)is.1943-555x.0000083

Lai, W. L., & Poon, C. S. (2012). Applications of Nondestructive Evaluation Techniques in Concrete Inspection. *HKIE Transactions, 19*(4), 34-41. doi:10.1080/1023697X.2012.10669003

Lai, W. W.-L., Dérobert, X., & Annan, P. (2017). A review of Ground Penetrating Radar application in civil engineering: A 30-year journey from Locating and Testing to Imaging and Diagnosis. *NDT & E International*.

Lai, W. W., Ho, M. L.-Y., Chang, R. K., Sham, J. F., & Poon, C.-S. (2017). Tracing and imaging minor water seepage of concealed PVC pipe in a reinforced concrete wall by high-frequency ground penetrating radar. *Construction and Building Materials, 151*, 840-847.

Lambot, S., Slob, E. C., van den Bosch, I., Stockbroeckx, B., & Vanclooster, M. (2004). Modeling of ground-penetrating radar for accurate characterization of subsurface electric properties. *IEEE Transactions on Geoscience and Remote Sensing, 42*(11), 2555-2568.

Leckebusch, J. (2003). Ground‐penetrating radar: a modern three‐dimensional prospection method. *Archaeological Prospection, 10*(4), 213-240.

Leckebusch, J., & Peikert, R. (2001). Investigating the true resolution and three-dimensional capabilities of ground-penetrating radar data in archaeological surveys: measurements in a sand box. *Archaeological Prospection, 8*(1), 29-40.

Léger, E., Saintenoy, A., & Coquet, Y. (2014). Hydrodynamic parameters of a sandy soil determined by ground-penetrating radar inside a single ring infiltrometer. *Water resources research, 50*(7), 5459-5474. doi:10.1002/2013wr014226

Leucci, G., & Negri, S. (2006). Use of ground penetrating radar to map subsurface archaeological features in an urban area. *Journal of Archaeological Science, 33*(4), 502-512. doi:10.1016/j.jas.2005.09.006

Leucci, G., Negri, S., & Carrozzo, M. T. (2003). Ground Penetrating Radar (GPR): an application for evaluating the state of maintenance of the building coating. *Annals of Geophysics, 46*(3).

Maas, C., & Schmalzl, J. (2013). Using pattern recognition to automatically localize reflection hyperbolas in data from ground penetrating radar. *Computers & Geosciences, 58*, 116-125. doi:https://doi.org/10.1016/j.cageo.2013.04.012

Marchesini, P., & Grasmueck, M. (2015). The impact of high-density spatial sampling versus antenna orientation on 3D GPR fracture imaging. *Near Surface Geophysics, 13*(2061). doi:10.3997/1873-0604.2015007

Metwaly, M. (2015). Application of GPR technique for subsurface utility mapping: A case study from urban area of Holy Mecca, Saudi Arabia. *Measurement, 60*, 139-145. doi:10.1016/j.measurement.2014.09.064

Millington, T. M., & Cassidy, N. J. (2010). Optimising GPR modelling: A practical, multi-threaded approach to 3D FDTD numerical modelling. *Computers & Geosciences, 36*(9), 1135-1144.

Nuzzo, L., Leucci, G., Negri, S., Teresa Carrozzo, M., & Quarta, T. (2002). Application of 3D Visualization Techniques in the Analysis of GPR data for Archaeology. *Annals of Geophysics, 45*(2).

Pérez-Gracia, V., Di Capua, D., González-Drigo, R., Caselles, O., Pujades, L., & Salinas, V. (2010). *GPR resolution in Cultural Heritage applications.* Paper presented at the Ground Penetrating Radar (GPR), 2010 13th International Conference on.

Pérez-Gracia, V., Di Capua, D., González-Drigo, R., & Pujades, L. (2009). Laboratory characterization of a GPR antenna for high-resolution testing: Radiation pattern and vertical resolution. *NDT & E International, 42*(4), 336-344.

Pérez-Gracia, V., González-Drigo, R., & Di Capua, D. (2008). Horizontal resolution in a non-destructive shallow GPR survey: An experimental evaluation. *NDT & E International, 41*(8), 611-620.

Porsani, J. L., Ruy, Y. B., Ramos, F. P., & Yamanouth, G. R. B. (2012). GPR applied to mapping utilities along the route of the Line 4 (yellow) subway tunnel construction in São Paulo City, Brazil. *Journal of Applied Geophysics, 80*, 25-31. doi:10.1016/j.jappgeo.2012.01.001

Ristic, A. V., Petrovacki, D., & Govedarica, M. (2009). A new method to simultaneously estimate the radius of a cylindrical object and the wave propagation velocity from GPR data. *Computers & Geosciences, 35*(8), 1620-1630.

Ruck, G. T., Barrick, D. E., Stuart, W. D., & Krichbaum, C. K. (1970). *Radar Cross Section Handbook. Volumes 1 & 2*: Plenum Press, New York.

586 Sagnard, F., Norgeot, C., Derobert, X., Baltazart, V., Merliot, E., Derkx, F., & Lebental, B. (2016). Utility
587 detection and positioning on the urban site Sense-City using Ground-Penetrating Radar systems.
588 *Measurement, 88*, 318-330. doi:10.1016/j.measurement.2016.03.044
589 Sham, J. F. C., & Lai, W. W. L. (2016). Development of a new algorithm for accurate estimation of GPR's wave
590 propagation velocity by common-offset survey method. *NDT and E International, 83*, 104-113.
591 doi:10.1016/j.ndteint.2016.05.002
592 Topczewski, L., Fernandes, F. M., Cruz, P. J., & Lourenço, P. B. (2007). Practical implications of GPR
593 investigation using 3D data reconstruction and transmission tomography. *Journal of Building*
594 *Appraisal, 3*(1), 59-76.
595 Xie, F., Wu, C. G.-W., Lai, W. W.-L., & Sham, J. F.-C. (2018). Correction of multi-frequency GPR wave velocity
596 with distorted hyperbolic reflections from GPR surveys of underground utilities. *Tunnelling and*
597 *Underground Space Technology, 76*, 76-91.
598 Zanzi, L., & Arosio, D. (2013). Sensitivity and accuracy in rebar diameter measurements from dual-polarized
599 GPR data. *Construction and Building Materials, 48*, 1293-1301.

600